ACS APPLIED MATERIALS & INTERFACES

Research Article

www.acsami.org

Nanoparticulate Mn_3O_4/VGCF Composite Conversion-Anode Material with Extraordinarily High Capacity and Excellent Rate Capability for Lithium Ion Batteries

Feng Ma, Anbao Yuan,* and Jiaqiang Xu

Department of Chemistry, College of Sciences, Shanghai University, Shanghai 200444, China

Supporting Information

ABSTRACT: In this work, highly conductive vapor grown carbon fiber (VGCF) was applied as an electrically conductive agent for facile synthesis of a nanoparticulate Mn_3O_4/VGCF composite material. This material exhibits super high specific capacity and excellent rate capability as a conversion-anode for lithium ion batteries. Rate performance test result demonstrates that at the discharge/charge current density of 0.2 A g^{-1} a reversible capacity of ca. 950 mAh g^{-1} is delivered, and when the current rate is increased to a high current density of 5 A g^{-1}, a reversible capacity of ca. 390 mAh g^{-1} is retained. Cyclic performance examination conducted at the current density of 0.5 A g^{-1} reveals that in the initial 20 cycles the reversible capacity decreases gradually from 855 to 747 mAh g^{-1}. However, since then, it increases gradually with cycle number increasing, and after 200 cycles an extraordinarily high reversible capacity of 1391 mAh g^{-1} is achieved.

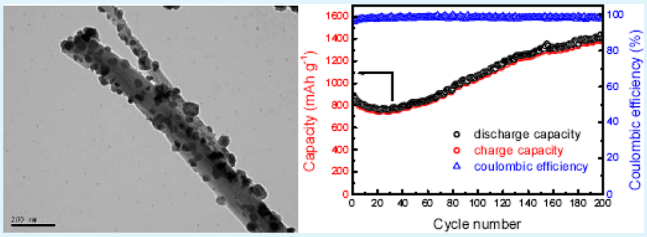

KEYWORDS: *nano-Mn_3O_4, vapor grown carbon fiber, composite, anode, lithium ion battery*

1. INTRODUCTION

Atmospheric pollution caused by combustion of fossil fuels and gas emission of automobiles, and so on, becomes more and more harmful to human beings, leading to severe environment issues, such as increased greenhouse effect, acid rain, and frequently encountered supercriterion of harmful fine-particulate-matter (PM 2.5) in the atmosphere. Hence, in the present situation, it is urgent to develop alternative clean energies for our society, for example, initiating large-scale applications of solar energy, wind energy, and zero-emission electric vehicles (EVs) or low-emission hybrid electric vehicles (HEVs). Lithium-ion batteries (LIBs) are considered promising candidates for EVs, HEVs, and other energy storage applications because of their high energy and power densities, long lifespan, and low self-discharge rate, etc. Now, LIBs are moving from small-sized mobile devices of information technology to large-scale EVs and energy storage systems.[1] To satisfy the requirements of practical applications, however, further studies on modification or improvement of LIBs' electrode materials should be carried out. Compared to the commercially used graphite anode with a relatively low theoretical capacity of 372 mAh g^{-1}, nanosized transition metal oxides MO (M = Fe, Co, Ni, etc.) have much higher specific capacities based on the conversion reaction involving reduction/oxidation of M and formation/decomposition of Li_2O upon cycling.[2]

Among various transition metal oxides, Mn_3O_4 has received much attention, owing to its high theoretical capacity (937 mAh g^{-1}), abundance of manganese source, low cost, and low toxicity. However, these advantages are always hindered by its intrinsically low electric conductivity (~10^{-8} to 10^{-7} S cm^{-1})[3] and huge volume swelling upon lithiation/delithiation, which may cause pulverization of electrode materials and deterioration of electric contact. Even doped with cobalt, the performance is still far from a desirable level.[4]

To overcome these drawbacks, various endeavors have been tried in recent years. One strategy is to synthesize Mn_3O_4 with a one/two-dimensional morphology or hollow/porous nanostructure.[5−15] These designs are based on the fact that the nanostructures can alleviate the strain in repeated discharge/charge cycling due to their nanosized dimension or voids among nanoparticles. Another approach to improve cycling and rate performances of Mn_3O_4 is to prepare Mn_3O_4/carbon composites. Different kinds of carbon have been employed, for instance, carbon nanotube,[16,17] reduced graphene oxide,[18−28] mesoporous carbon,[3,29] electrospinning-polyacrylonitrile-nanofiber derived porous carbon nanofiber,[30−32] nanosized carbon black and micron-sized graphitic flakes[33] and hydrothermally polyvinylpyrrolidone derived carbon.[34] These modifications can increase the electrical conduction of the electrode materials and/or improve the stability of the electrode framework. For example, graphene-supported mesoporous Mn_3O_4 nanosheet composite can present a high reversible capacity of ca. 900 mAh g^{-1} at the current density of 0.4 A g^{-1} and a good rate-capacity

Received: July 29, 2014
Accepted: September 23, 2014
Published: September 23, 2014

retention of around 500 mAh g^{-1} at a higher current density of 4 A g^{-1}.[24] MnO_x (Mn_3O_4 with a small portion of MnO) nanocrystals impregnated in ordered mesoporous carbon (OMC) nanorods can exhibit a stable cycling performance (>950 mAh g^{-1} after 50 cycles at a current density of 0.2 A g^{-1}).[29]

These advancements reveal that nanosized Mn_3O_4 particles with micronano-structured morphology or being supported on an electrically conductive skeleton may promise good rate- and cycling-performances. Vapor grown carbon fiber (VGCF) by chemical vapor deposition (CVD) has been used as conductive additive for fabrication of $Li_{4/3}Ti_{5/3}O_4$ anode by physical blend[35] and $Li_4Ti_5O_{12}$/VGCF composite anode by ball milling,[36] and $LiMn_xFe_{1-x}PO_4$/VGCF core−sheath nanowire composite cathodes by electrospinning method[37,38] for lithium-ion batteries recently. However, as far as we know, there is no report of Mn_3O_4/VGCF composite up to now.

In the present work, a Mn_3O_4/VGCF composite material was synthesized via a two-step synthetic route starting with the reaction taken place in the mixed aqueous solution of potassium permanganate and manganese acetate in the presence of VGCF to form MnO_2/VGCF composite (precursor), followed by heat treatment of the precursor at 450 °C in an inert atmosphere. The electrochemical performance of the composite was investigated as an anode material for lithium ion battery. Unlike the carbon fibers derived from thermal carbonization of electrospinning-polyacrylonitrile at a relatively low temperature of 700 °C (which has a relatively low degree of graphitization),[30−32] the VGCF used herein has a high electric conductivity of 10^4 S m^{-1} and a one-dimensional structure of solid fibers, and therefore, a better enhancement of electrical conduction and a better improvement of performance of the composite material would be expected.

2. EXPERIMENTAL SECTION

2.1. Synthesis of Material. Vapor grown carbon fiber (0.075 g; VGCF, Showa Denko Carbon Inc., Japan) was dispersed in 70 mL of deionized water and sonicated for 20 min. Then, 15 mL of 0.267 M potassium permanganate ($KMnO_4$, 4 mmol) aqueous solution was added to the VGCF suspension under magnetic stirring and was continuously stirred at 40 °C for 5 h in favor of adsorption of MnO_4^- ions on the surface of VGCF. Subsequently, 20 mL of 0.1 M manganese acetate ($Mn(OAc)_2$, 2 mmol) aqueous solution was slowly added to the above $KMnO_4$−VGCF suspension with a dropping speed of ca. 1 mL min^{-1}, and the mixed suspension was subjected to continuous stirring at 40 °C for 24 h to ensure completion of the reaction. After that, the solid product was filtered out and washed with deionized water and ethanol each for 5 times. After drying in a drybox at 80 °C for 24 h, the red brown powder was obtained. Finally, the powder was placed in a tube furnace, and the temperature was increased up to 450 °C with a heating rate of 2 °C min^{-1} under the flow of argon gas and kept at this temperature for 3 h before it was cooled to room temperature. Thus, the Mn_3O_4/VGCF composite material was obtained. The preparation process is depicted in Scheme 1.

2.2. Characterization of Material. X-ray diffraction (XRD) patterns were collected on a Rigaku D/max 2200 X-ray diffractometer with Cu Kα radiation (40 kV/40 mA) at a scan rate of 6° min^{-1} over the 2θ range 10−90°. Morphological observations were performed using field-emission scanning electron microscope (FE-SEM, Hitachi S-4800, and JEOL JSM-6700F) and transmission electron microscope (TEM, JEOL JEM-200CX). Carbon (VGCF) content was analyzed by use of an elemental analyzer (VARIO EL III Elementar Analysensysteme, GmbH, Hanau, Germany).

2.3. Electrochemical Measurements. Working electrode was fabricated by mixing active material (Mn_3O_4/VGCF or pure VGCF), acetylene black conductive agent and sodium alginate ($C_6H_7O_6Na$) binder in the weight ratio of 75:15:10 with a few drops of deionized water. The resultant slurry was coated onto a copper foil current collector with a doctor blade and dried at 80 °C in vacuum overnight. CR2016 coin-type half-cells were assembled in an argon filled glovebox (MIKROUNA Super 1220/750, Mikrouna (China) Co., Ltd., with O_2 and H_2O concentration <1 ppm) using the fabricated working electrodes and metallic lithium foil electrodes and 1 M $LiPF_6$ dissolved in a mixture of ethylene carbonate (EC), dimethyl carbonate (DMC) and methyl ethyl carbonate (EMC) (1:1:1 v/v/v) as electrolyte. All the electrochemical measurements were conducted at room temperature on the assembled CR2016 coin-type cells, where the Mn_3O_4/VGCF or pure VGCF electrode served as the working electrode and the lithium foil as the counter electrode as well as reference electrode. Specifically, electrochemical impedance spectroscopy (EIS) and cyclic voltammetry (CV) measurements were performed on CorrTest CS330 Electrochemical Workstation (Wuhan, China). Galvanostatic discharge/charge tests were carried out on Land CT2001A autocycler (Wuhan, China).

Scheme 1. Schematic Diagram for Preparation of Mn_3O_4/VGCF Composite

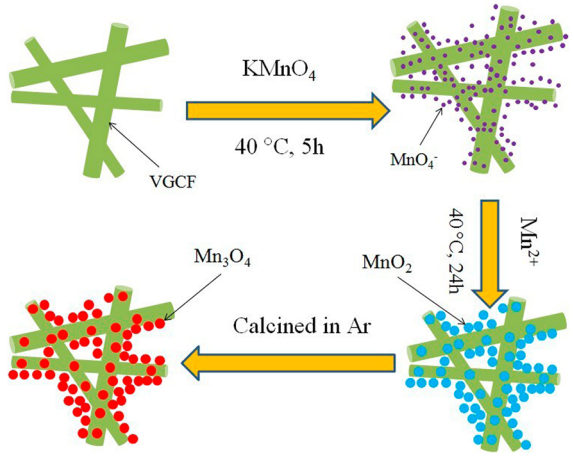

3. RESULTS AND DISCUSSION

3.1. Structural and Morphological Analysis. XRD patterns of the VGCF, MnO_2/VGCF precursor and Mn_3O_4/VGCF composite are shown in Figure 1. As can be seen, the VGCF shows an intensive and sharp peak at 2θ = 26.4° that is in well agreement with the (002) reflection of the graphite (PDF 41-1487), suggesting a high degree of graphitization. A carbon material with this feature is believed to be highly

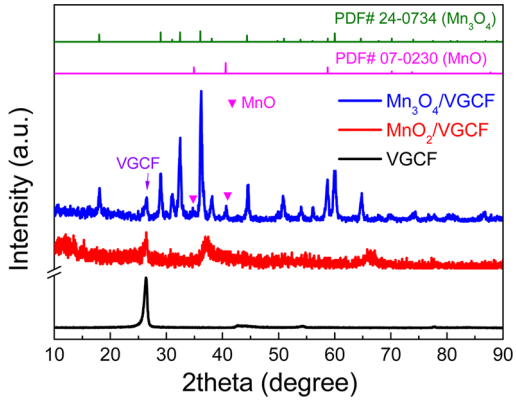

Figure 1. XRD patterns of VGCF, MnO_2/VGCF precursor and Mn_3O_4/VGCF composite.

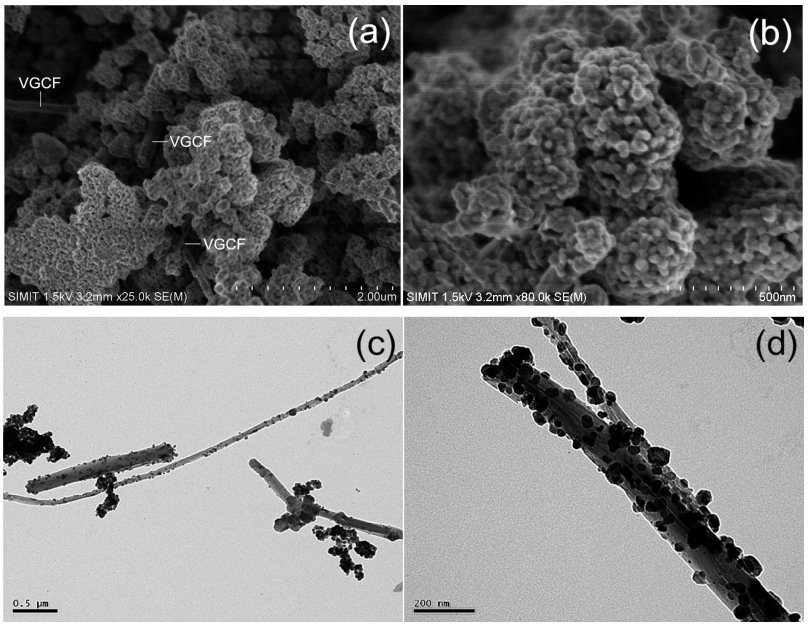

Figure 2. (a, b) SEM and (c, d) TEM images of Mn_3O_4/VGCF composite.

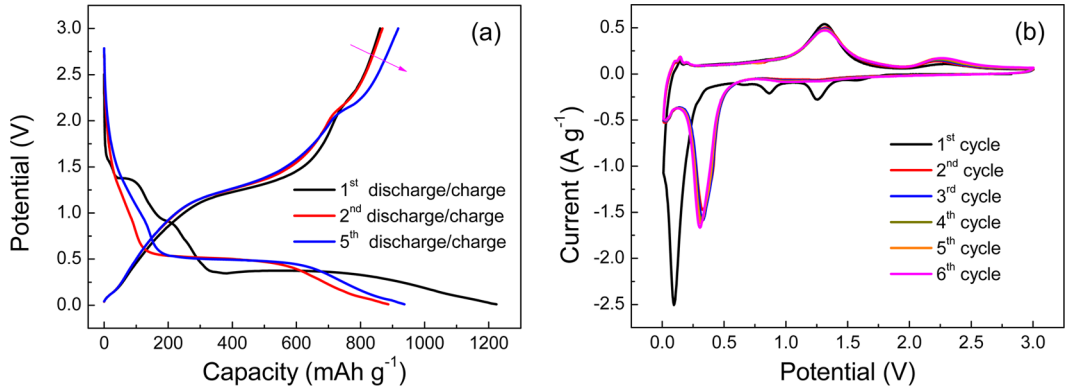

Figure 3. (a) Selected discharge/charge curves at the current density of 0.1 A g^{-1}. (b) CVs at the scan rate of 0.2 mV s^{-1} of Mn_3O_4/VGCF composite.

conductive for electron transport. The reflections of the MnO_2/VGCF at around 2θ = 12°, 26°, 37° and 67° should be ascribed to the layered δ-type K-birnessite MnO_2 (potassium manganese oxide hydrate, PDF 80-1098). The strong diffraction of VGCF in this composite would overlap with the diffraction of MnO_2 at ca. 26°. All the peaks of the Mn_3O_4/VGCF composite should be indexed to the tetragonal-phase hausmannite-type Mn_3O_4 (PDF 24-0734, space group $I4_1/amd$), except for the two weak reflections located at 34.4° and 40.5°, which are the characteristic diffractions of (111) and (200) planes of the cubic-phase manganosite-type MnO (PDF 07-0230, space group $Fm3m$). In addition, the weak reflection at 26.4° should be assigned to VGCF. Thus, it can be concluded that heat treatment of the MnO_2/VGCF precursor at 450 °C for 3 h under the atmosphere of flow argon can lead to decomposition of MnO_2 and thereby formation of Mn_3O_4/VGCF composite with a small amount of MnO impurity phase.

Figure 2 shows the SEM and TEM images of the Mn_3O_4/VGCF composite with different magnifications. VGCF fibers are embedded in the congeries of Mn_3O_4 particles with part of them being exposed to be seen clearly (Figure 2a). Mn_3O_4 nanoparticles with the size of around 40 nm are reunited to form aggregates (Figure 2b). As shown in Figure 2c and d, the VGCF has different diameters (ca. 50 to 200 nm) and lengths. A lot of Mn_3O_4 nanoparticles (typically 30 to 50 nm) are homogeneously dispersed on and intimately combined with the surface of VGCF (Figure 2d). Elemental analysis revealed that the carbon content in the Mn_3O_4/VGCF composite is 13.52 wt %. The intimately combined Mn_3O_4 nanoparticles on the surface of VGCF should be the result of in situ heating-conversion of MnO_2 which is formed from in situ direct redox reaction of MnO_4^- with the surface of VGCF, and/or the redox reaction of adsorbed MnO_4^- (on the surface of VGCF) with Mn^{2+} in the solution.

3.2. Electrochemical Performance. In this paper, we denote the reduction process (lithiation) of a Mn_3O_4/VGCF electrode as discharge, while the oxidation process (delithiation) is denoted as charge. This type of denotation (or definition) is identical to that of the corresponding coin-type cell. So, a fresh Mn_3O_4/VGCF electrode should be initially discharged to the down cutoff potential of 0.01 V vs Li^+/Li (or the down cutoff voltage of 0.01 V for the coin-type cell) and then recharged to the up cutoff potential of 3 V vs. Li^+/Li. All current densities and specific capacities are calculated based on

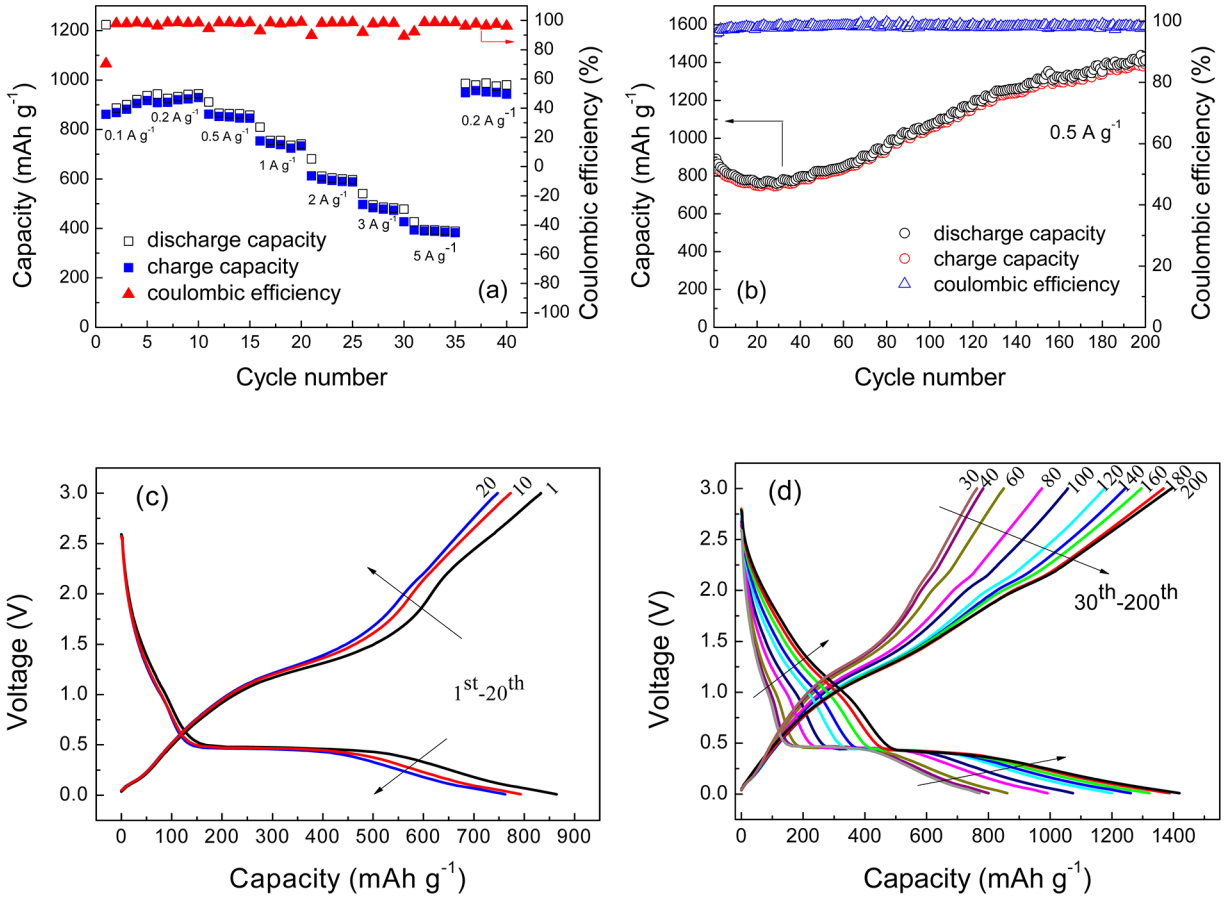

Figure 4. (a) Rate performance. (b) Cycle performance at the current density of 0.5 A g^{-1}. (c, d) Selected discharge/charge curves at 0.5 A g^{-1} of Mn_3O_4/VGCF composite.

the weight of Mn_3O_4/VGCF composite active material (or the weight of VGCF for the pure VGCF electrode).

Figure 3a shows selected discharge/charge curves (first, second and fifth cycles) of a fresh Mn_3O_4/VGCF electrode (coin-type half cell) at a current density of 0.1 A g^{-1} between 0.01 and 3 V (vs Li^+/Li). As can be seen, the fist discharge capacity (1223.6 mAh g^{-1}) is much higher than the first charge capacity (861.1 mAh g^{-1}), giving a low Coulombic efficiency of 70.4% due to the initially and prevalently available decomposition of electrolyte solvent and formation of a solid electrolyte interface (SEI) layer upon first discharging as well as the irreversible reaction upon recharging. This phenomenon has been commonly observed for Mn_3O_4 or its composite[7,9,22] and other transition metal oxides such as α-Fe_2O_3, NiO, and Co_3O_4.[39−41] Two short plateaus at ca. 1.35 and 0.90 V can be observed in the first discharge curve, which correspond well to the two cathodic peaks at ca. 1.30 and 0.85 V, respectively, in the cyclic voltammogram (CV) for the first cycle shown in Figure 3b. In addition, a weak current peak at around 1.6 V could also be observed in the CV for the first cathodic scan (which can be seen more clearly in Figure 6). These observations are related to the initial lithiation of Mn_3O_4 to MnO and Li_2O (perhaps via formation of an intermediate product of $LiMn_3O_4$) and the initial cathodic process of VGCF (see Figure S1 and S2, Supporting Information (SI)) existing in the composite accompanied by the initial decomposition of electrolyte solvent (formation of a SEI layer). The long discharge plateau at ca. 0.37 V and the succeeding voltage dropping correspond to the intensive and sharp cathodic peak at ca. 0.10 V in the CV, which should be attributed mainly to the prior-period conversion of MnO to metallic Mn and Li_2O in addition to the later-stage decomposition of electrolyte solvent. During the first recharging, the long quasi-plateau at around 1.25 V and the succeeding voltage sloping above 2 V observed in the first charge curve correspond to the strong anodic peak at ca. 1.35 and the shoulder peak at around 2.25 V, respectively, in the first anodic CV scan. The strong anodic peak at ca. 1.35 V should be ascribed to the reverse oxidation of Mn (coupled with the decomposition of Li_2O) to MnO,[42−44] and the shoulder at the higher potential at around 2.25 V, the intensity of which increases with increasing cycle number may be associated with a further oxidation of MnO to a higher oxidation state of Mn species. This phenomenon has been observed previously for some Mn_3O_4 and Mn_3O_4/conductive carbon composite materials.[7,10,12,21,22,28,29] Correspondingly, a very weak and broad peak occurred at around 1.10 V in the subsequent reverse CV scan (which can be seen more clearly in Figure 6) should be attributed to the reduction of the higher valence Mn species back to MnO, suggesting a partial reversibility of this redox reaction. However, in the second cycle of CV scan, the intensity of the main cathodic peak corresponding to MnO reduction is decreased obviously and shifted to a higher potential of ca. 0.35 V due to the structure changes during the initial lithiation process in the first cycle, which is a common phenomenon to manganese oxide based electrodes.[12] This change of CV is in accordance with the corresponding discharge plateau moved to a higher potential near 0.5 V during the second discharging.

In addition to the observations discussed above, since the second CV cycle, an obvious cathodic peak at the end potential of 0.01 V can be seen clearly due to the obvious positive shift of the main cathodic peak. This peak should be correlated with the reductive decomposition of electrolyte at a low potential coupled with the lithiation of VGCF (Figure S2, SI). Correspondingly, a very small but still recognizable anodic peak at ca. 0.25 V could also be observed due to the delithiation of VGCF (Figure S2, SI). Thereafter, the essential characteristics for the subsequent cycles are continually repeated time after time.

Rate performance of the Mn_3O_4/VGCF composite from 0.1 to 5 A g^{-1} is shown in Figure 4a. The first discharge and charge capacities at 0.1 A g^{-1} is 1223.6 and 861.1 mAh g^{-1}, respectively, exhibiting a low Coulombic efficiency of 70.4%. However, the Coulombic efficiency is greatly increased to 97.9% in the second cycle. Besides, a successive increasing of reversible capacity is found during the initial 5 cycles at 0.1 A g^{-1}, and the maximum capacity achieved at 0.2 A g^{-1} is, on the contrary, a little higher than that obtained at 0.1 A g^{-1} due to the continued increasing of capacity. Since 0.5 A g^{-1}, the capacity decreases gradually with increasing current density. Nevertheless, a specific capacity of ca. 390 mAh g^{-1} (a little larger than the theoretical capacity of graphite, 372 mAh g^{-1}) is still retained even at a high current density of 5 A g^{-1}, suggesting a good rate capability. The high electronic conductivity of the combined VGCF with high aspect ratio should be responsible for the good rate capability due to the enhancement of electron transport in the electrode. Even more, when the current density comes back again to 0.2 A g^{-1}, a specific capacity of ca. 950 mAh g^{-1} is maintained, which is a little higher than the previously obtained capacity at the same current density, suggesting an excellent cyclic stability.

After the rate performance test, the Mn_3O_4/VGCF composite was subjected to cycle performance test at a discharge/charge current density of 0.5 A g^{-1}, and the result is given in Figure 4b). The initial charge capacity is 855 mAh g^{-1}, and thereafter, the capacity decreases gradually. After 20 cycles, the capacity is decreased to a minimum value of 747 mAh g^{-1}. However, it is interesting that a gradual increase of capacity is observed from that time on. After 200 cycles, a high capacity of 1391 mAh g^{-1} is achieved. In addition, the cycle performance conducted at a lower current density of 0.2 A g^{-1} also presents a similar capacity increasing behavior (Figure S3, SI). To the best of our knowledge, this is the highest specific capacity compared with the previously reported values for Mn_3O_4 and its composites (Table S1, SI). To know the contribution of VGCF to the capacity of the composite, the rate capability and cyclability at 0.5 A g^{-1} of a pure VGCF electrode were also performed (see Figure S4 and S5, SI). The initial specific capacity of the VGCF at 0.5 A g^{-1} is only 185.3 mAh g^{-1}. After 200 cycles, the specific capacity is increased to 240 mAh g^{-1}. Such a low increment in capacity cannot explain the capacity increasing of the Mn_3O_4/VGCF composite.

The theoretical capacity of Mn_3O_4 is 937 mAh g^{-1} based on the reaction

$$Mn_3O_4 + 8Li^+ + 8e^- \Leftrightarrow 3Mn + 4Li_2O$$

However, HRTEM study of the oxidized product of Mn_3O_4 electrode recharged to 3 V conducted by Fang et al. demonstrated that Mn could only be oxidized to MnO since the first recharge.[42] If MnO is taken as the only end oxidized product, the theoretically reversible capacity of Mn_3O_4 should be as low as 703 mAh g^{-1} (937 × 6/8 = 703). However, if MnO would be further oxidized to MnO_2, the theoretically reversible capacity of Mn_3O_4 should be as high as 1405.5 mAh g^{-1} (937 × 12/8 = 1405.5). Lowe and co-workers use in operando nondestructive synchrotron X-ray diffraction and X-ray absorption spectroscopy (XAS) techniques to directly observe the conversion reaction of a Mn_3O_4 anode.[43] They proposed that more than 150 mAh g^{-1} contribution corresponding to the low-voltage range in the discharge curve may be caused by a capacitive-like charge storage. Yonekura et al. further studied the conversion reaction in different depths of discharge (DOD) and suggested that when the DOD reached 75%, the remaining capacity was not caused by Mn species but by the degradation of electrolyte. This leads to the formation of a polymer-like network encapsulating the Li_2O matrix which separate the Mn clusters. The polymer-like network may be an origin of the capacitive-like extra capacity.[44] These ways of interpretations are similar to those suggested in earlier reports about CoO and other Co-based compounds.[45,46] They considered that the contribution of ca. 150 mAh g^{-1} corresponding to the low-voltage range should be associated with the reversible formation/dissolution of gel-like polymeric species at low potential in alkyl carbonate solution, which is unique in the field of Li-based rechargeable batteries. The observed pseudocapacitive behavior was believed to be originated from the in situ formation of highly reactive pristine metallic nanograins that promotes the growth of a conducting-type polymeric film.

The phenomenon of voltage drop observed in the last stage of galvanostatic discharging herein may be explained as follows. Before this stage, the main reaction is the multiphase conversion of MnO to Mn, and hence, a potential plateau can be observed. According to the previous study,[44] as this reaction proceeds, the decomposition of electrolyte would be catalytically enhanced by the produced metallic Mn clusters. The valence number of Mn species was confirmed to be near zero at the end of the discharge plateau and remained unchanged up to the end of fully discharged state (near 0 V). Meanwhile, the thickness of the SEI layer was greatly increased to 20−30 nm and eventually covered the Mn−Li_2O nanopartcles. Based on these results, the authors proposed that the last stage discharging (voltage dropping after the plateau) is related to electrolyte decomposition, but they did not explain why the last-stage voltage profile would take the shape of a continuous dropping of voltage. With reference to their findings, we speculate that, at the end of the plateau, most of the MnO are converted to Mn clusters and Li_2O nanoparticles and the further conversion of the remaining MnO would become more difficult because the pathway for Li^+ ions diffusion from electrolyte to MnO is increased. Consequently, the diffusion polarization is also increased, resulting in voltage dropping. Meanwhile, the electrolyte decomposition is promoted by the catalysis of the 3d-group metallic Mn clusters. However, as the decomposition proceeds, the thickness of the SEI layer continues to increase, which would hinder the catalytic role of Mn and lead to continuous voltage dropping.

To better understand the capacity degradation in the initial 20 cycles and the subsequent capacity increase in the remaining cycles (Figure 4b), the selected discharge/charge curves are displayed in Figure 4(c and d), which shows clearly the evolution of discharge and charge curves during repeated cycling. As can be seen in Figure 4c, both the capacities of the discharge plateau at ca. 0.5 V and the charge quasi-plateau at

around 1.4 V all decrease with increasing cycle number. Therefore, the capacity drop corresponding to the reciprocal conversion reaction between MnO and Mn should be responsible for the capacity degradation in the initial 20 cycles.

From 30 to 200 cycles, as shown in Figure 4d, for the charging process, the charge capacities corresponding to both the high voltage range (above 2 V) and the low voltage range (below 2 V) increase gradually with increasing cycle number. For the discharging process, the discharge capacities corresponding to both the high voltage range (above 0.5 V) and the low voltage range (below 0.5 V) increase gradually with increasing cycle number, while the length of the discharge plateau at 0.5 V decreases slightly with increasing cycle number. This plateau is commonly believed to be related to the conversion reaction of MnO to metallic Mn. From these results, it can be concluded that the increase in capacity is related to the electrode processes corresponding to the high voltage range as well as the low voltage range. Both the electrode processes account for the total increment of capacity. The suggested evolution of manganese oxide active material at fully charged state upon long-term discharge/charge cycling is shown in Scheme 2 to help understand the increase of capacity with cycle number (the detailed analysis and discussion will be presented as follows).

Scheme 2. Schematic Diagram for Suggested Evolution of Manganese Oxide Active Material at Fully Charged State upon Long-Term Discharge/Charge Cycling

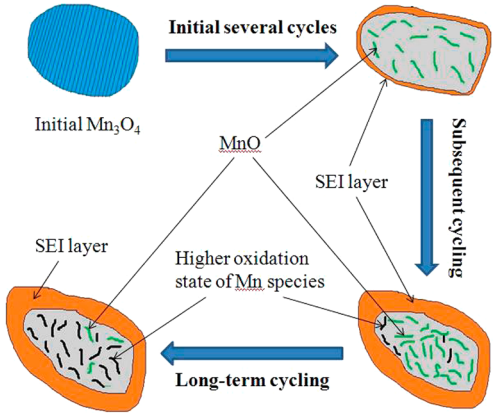

To further elucidate the phenomenon of capacity rising during cycling, electrochemical impedance spectroscopy (EIS) and CV measurements were performed on the Mn_3O_4/VGCF electrode after 100 discharge/charge cycles at 0.5 A g^{-1}. The EIS was measured at the charged state (fully charged to 3 V and then rested for several hours before measurement), and the CV was recorded at a scan rate of 0.2 mV s^{-1}. The Nyquist plot of the EIS is presented in Figure 5 in comparison with the pure VGCF and the Mn_3O_4/VGCF each cycled for initial 5 cycles at 0.1 A g^{-1}, and the inset shows the close-up view of EIS at the high frequency region. As shown, the Nyquist plot of the pure VGCF consists of a pressed semicircle at the high-frequency region and a slopping line at the low-frequency region, while the Nyquist plots of the Mn_3O_4/VGCF consist of a high-frequency very small arc and a medium-frequency arc followed by a low-frequency line. The high-frequency arc should be attributed to Li^+ ions migration through the SEI layer, and the medium-frequency arc is related to charge transfer at the electrode/electrolyte interface, and the low-frequency line

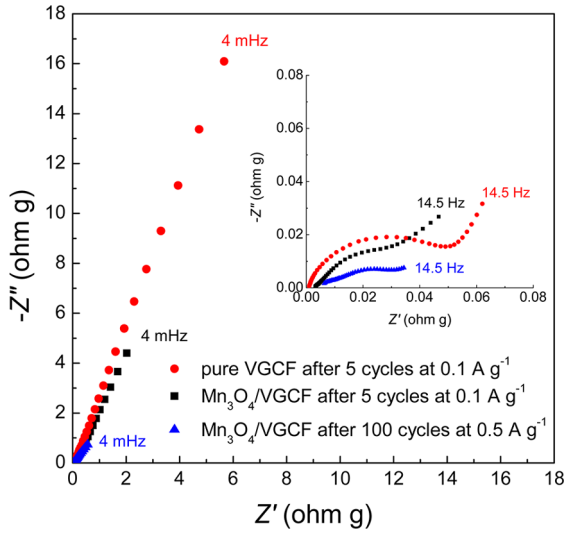

Figure 5. Nyquist plots at charged state of Mn_3O_4/VGCF composite after 100 discharge/charge cycles at 0.5 A g^{-1} in comparison with the pure VGCF and the Mn_3O_4/VGCF each cycled for initial 5 cycles at 0.1 A g^{-1}. Inset showing the close-up view of EIS at high frequency region.

represents ionic diffusion in solid. We can see from the inset that the ohmic resistance of the VGCF electrode is very small (0.001 ohm g) owing to its excellent electrical conduction. The ohmic resistances of the Mn_3O_4/VGCF electrode after initial 5 cycles at 0.1 A g^{-1} and after 100 cycles at 0.5 A g^{-1} are ca. 0.003 and 0.005 ohm g, respectively. These values are relatively small, although they are somewhat larger than that of the VGCF electrode. This is due to the enhancement of electrical conduction by incorporation of the VGCF and should be responsible for the good rate capability presented in Figure 4a. Compared with the Mn_3O_4/VGCF electrode after initial 5 cycles at 0.1 A g^{-1}, the charge transfer resistance and the overall impedance of the Mn_3O_4/VGCF electrode after 100 cycles at 0.5 A g^{-1} are reduced, suggesting a increased electrochemical reactivity of the electrode reaction taken at the state of a high potential. By comparison, the diffusion impedances of the Mn_3O_4/VGCF electrode are obviously larger than the charge transfer resistances, indicating that the reaction kinetics is essentially dominated by the diffusion process. The large voltage gap between the charge curve and the discharge curve which is commonly observed in metal oxide conversion anodes may be correlated to the very slow diffusion process.

CVs of the Mn_3O_4/VGCF electrode after 100 discharge/charge cycles at 0.5 A g^{-1} (two cycles) is shown in Figure 6 in comparison with the CVs of the fresh Mn_3O_4/VGCF electrode (initial three cycles). As can be seen, the intensity of the anodic peak at a higher potential of ca. 2.25 V for the fresh electrode increases and negatively shifts gradually with increasing cycle number. After 100 discharge/charge cycles at 0.5 A g^{-1}, this peak current is increased dramatically and obviously shifted to a lower potential of ca.2.12 V. Correspondingly, a broad cathodic peak at ca. 1.10 V can be observed clearly. These results suggest that the reactivity of the redox reaction between MnO and the higher-valence Mn species would increase gradually with increasing cycle number. Besides, the enclosed area under the CV for the cycled electrode is obviously increased compared with the fresh electrode although the intensities of the main redox peaks for the conversion reaction between Mn and MnO

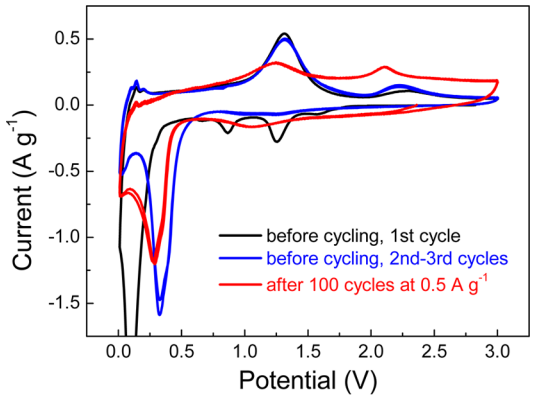

Figure 6. CVs of Mn_3O_4/VGCF electrode after 100 discharge/charge cycles at 0.5 A g^{-1} in comparison with CVs of fresh Mn_3O_4/VGCF electrode at the scan rate of 0.2 mV s^{-1}.

are decreased. This may suggest an increasingly rise of capacitive capacity contribution upon repeated discharge/charge cycling in addition to the capacity contribution offered by the above-discussed redox reaction taken place at higher potential range due to gradually pulverization of the electrode material. By carefully observing the CVs, we can find that the increase in charge capacity upon cycling originates from the charge increase in high potential range, which is mainly due to the further oxidation of MnO to a higher oxidation state. The increase in discharge capacity should be attributed to two factors, that is, the reduction of the higher-valence Mn species to MnO in the potential range above 0.5 V and the low-potential-range capacity contribution below 0.25 V. These results are well in agreement with the evolution of discharge/charge curves observed in Figure 4d. The proposed further oxidation of MnO to a higher oxidation state herein can also be supported by the reports for Mn_3O_4 and Mn_3O_4-based composite materials,[7,10,12,21,22,28,29] mischcrystal Mn_3O_4–Mn_2O_3/graphene composite material,[47] and MnO/graphene composite material.[48] These reported materials have a common denominator, namely, either a MnO_x/conductive carbon composite material (majority) or a pristine Mn_3O_4 material with a peculiar morphology.

Ex-situ Raman analysis of the Mn_3O_4/graphene composite electrode at various voltages in the first and second cycles demonstrated that when it was initially discharged to 0.5 V only a small amount of Li_2CO_3 (formed from Li_2O exposed to air and reacted with CO_2 and moisture) was detected.[21] However, when it was fully discharged to 0.001 V, the peak intensities of the Li_2CO_3 Raman features were dramatically increased due to the preferred formation of SEI layer at potentials below 0.5 V. On the contrary, when it was first recharged to 2 V, the intensities of the Li_2CO_3 features were obviously reduced, and even more, when it was fully recharged to 3 V, the Raman features of Li_2CO_3 almost disappeared. In the second discharge/charge cycle, the phenomenon recurred. These results suggest that the formation of SEI preferably takes place at low potentials below 0.5 V and the reversible decomposition of the SEI tend to take place at high potentials above 2 V. In addition, the Raman analysis result indicated that when the electrode was first charged to 3 V, the electrode active material was transformed into MnO_x ($x \sim 2$) instead of the initial Mn_3O_4.

With reference to previous studies and based on our findings, we propose that, in our case, owing to the distinct enhancement of electrical conduction offered by the intimately combined and highly conductive VGCF as well as its acting as a buffer matrix in the composite electrode, along with the nanostructured nature of the Mn_3O_4 active material, the reactivity, reversibility, kinetics characteristics, and, therefore, the utilization of active material of the conversion reaction could be remarkably improved. On this condition, the reactivity of the high-potential reversible reaction between MnO and the higher oxidation state of Mn species could continuously increase upon repeated discharge/charge cycling. The extra oxygen for the formation of the higher-valence Mn species may be supplied from the decomposition of Li_2CO_3 available in the SEI layer at higher potentials upon charging.

In order to observe the morphology and detect the phase composition of the Mn_3O_4/VGCF electrode at fully charged state after discharge/charge cycled at 0.5 A g^{-1} for 200 cycles, the cycled electrode (fully charged to 3 V) was separated from the coin-type cell and the extra electrolyte was absorbed by toilet paper and then subjected to SEM observation and XRD analysis. The separated disc-type electrode and the Celgard separator are shown in Figure S6 (SI). As can be seen, a layer of gel-like film (pale yellow color) is formed on the surface of the separator (the side facing to the Mn_3O_4/VGCF electrode). A fraction of the disc-type electrode was cut for SEM observation and the remainder was utilized for XRD analysis. Figure 7(a and b) shows the SEM images of the Mn_3O_4/VGCF electrode before (as-prepared fresh electrode) and after cycling at 0.5 A g^{-1} for 200 cycles. As shown, after 200 cycles, the active material is agglomerated into micron-sized (ca. 3 to 4 μm) particles with smooth surface, which is different from the case before cycling. In fact, the particles are composed of numerous nanowires (with a diameter of ca. 25 nm) interwoven each other looking like an intertexture with many micropores (Figure S8, SI). This observation is in accordance with the

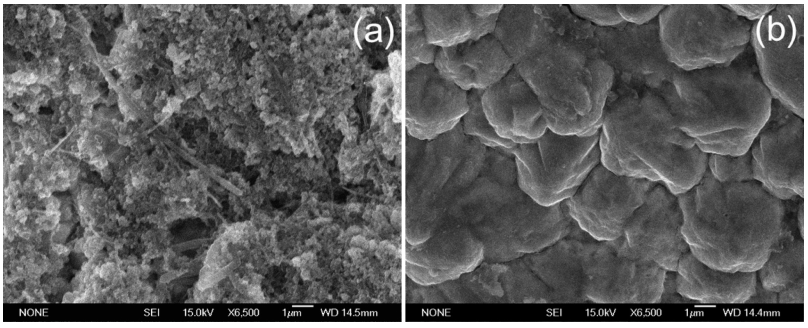

Figure 7. SEM images of Mn_3O_4/VGCF electrode (a) before cycling and (b) at charged state after 200 cycles at 0.5 A g^{-1}.

microcosmic conversion reaction model proposed by Yonekura et al.[44] Thus, it could be speculated that through cycling, the initial Mn_3O_4 nanoparticles would pulverize to superfine nanowires and then spontaneously agglomerate into micron-sized particles due to their high surface energy. These particles would be covered by the SEI related gel-like film seen in Figure S6, SI. The unseen VGCF should be embedded in the micron-sized particles. Owing to the incorporated VGCF as conductive framework, the pulverized active material would still maintain good conductivity.

Figure 8 shows the XRD patterns of the Mn_3O_4/VGCF electrode before and after being cycled at 0.5 A g^{-1} for 200 cycles in comparison with the as-prepared Mn_3O_4/VGCF material. Here, only the patterns within the 2θ range from 10 to 42 °C are displayed to avoid the interference of copper foil current collector. The whole patterns are presented in Figure S9 (SI). As shown in Figure 8, compared with the as-prepared Mn_3O_4/VGCF material, the diffractions of the fresh Mn_3O_4/VGCF electrode (before cycling) are very weak due to the too small amount of Mn_3O_4 available in the disc-type electrode. Nevertheless, a very weak reflection of the (211) plane at 36.08° could be observed. However, for the cycled Mn_3O_4/VGCF electrode, no reflections of active material could be observed except for the several reflections of Li_2CO_3, suggesting the amorphous nature of the active material. This result is in agreement with the previous study, where no reflections could be observed in the XRD pattern of a fully charged Mn_3O_4/graphene active material.[21] The detected Li_2CO_3 in the XRD pattern are originated from the electrode exposure to air for a long time before XRD analysis, which can be confirmed by the observation of a lot of small white spots (Li_2CO_3 particles) distributed on the surface of the electrode (Figure S10, SI).

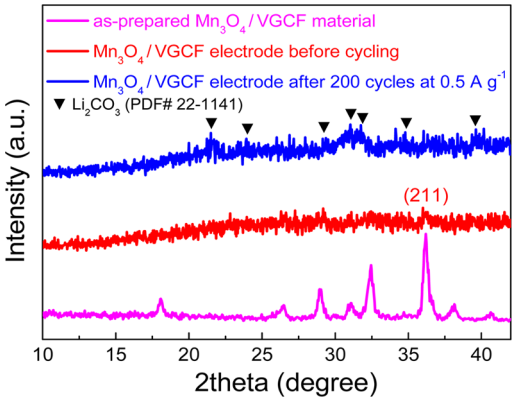

Figure 8. XRD patterns of Mn_3O_4/VGCF electrode at charged state before and after 200 cycles at 0.5 A g^{-1} in comparison with as-prepared Mn_3O_4/VGCF material.

4. CONCLUSIONS

In summary, a nanoparticulate Mn_3O_4/VGCF composite anode material for lithium ion batteries was prepared by a facile approach and characterized by XRD, SEM, and elemental analysis instrumentalities. Its electrochemical performance was investigated by EIS, CV, and galvanostatic discharge/charge methods. Electrochemical experimental results demonstrated that this material possesses super high specific capacity and excellent rate capability. A phenomenon of continuous increasing in capacity upon repeated discharge/charge cycling was found at the current densities of 0.2 and 0.5 A g^{-1}, respectively. An extraordinarily high reversible capacity of 1391 mAh g^{-1} is achieved after 200 cycles at the current density of 0.5 A g^{-1}. This phenomenon should be attributed to the increasingly enhanced reactivity of the extra reversible conversion reaction between MnO and the higher oxidation state of Mn species upon repeated cycling. The combined highly conductive VGCF should be responsible for the promotion and enhancing of the extra reaction.

■ ASSOCIATED CONTENT

Supporting Information

Discharge and charge curves, CVs, rate performance, and cycle performance of VGCF. Cycle performance of Mn_3O_4/VGCF at 0.2 A g^{-1}. Photograph, enlarged SEM image, and XRD pattern of Mn_3O_4/VGCF electrode after 200 cycles. This material is available free of charge via the Internet at http://pubs.acs.org.

■ AUTHOR INFORMATION

Corresponding Author

*Tel.: +86 21 66138003. Email: abyuan@shu.edu.cn.

Notes

The authors declare no competing financial interest.

■ ACKNOWLEDGMENTS

Instrumental Analysis and Research Center of Shanghai University is gratefully acknowledged for XRD, SEM, and TEM experiments.

■ REFERENCES

(1) Kim, T.-H.; Park, J.-S.; Chang, S. K.; Choi, S.; Ryu, J. H.; Song, H.-K. The Current Move of Lithium Ion Batteries towards the Next Phase. *Adv. Energy Mater.* **2012**, *2*, 860−872.

(2) Poizot, P.; Laruelle, S.; Grugeon, S.; Dupont, L.; Tarascon, J.-M. Nano-Sized Transition-Metal oxides as Negative-Electrode Materials for Lithium-Ion Batteries. *Nature* **2000**, *407*, 496−499.

(3) Li, Z. Q.; Liu, N. N.; Wang, X. K.; Wang, C. B.; Qi, Y. X.; Yin, L. W. Three-Dimensional Nanohybrids of Mn_3O_4/ordered Mesoporous Carbons for High Performance Anode Materials for Lithium-Ion Batteries. *J. Mater. Chem.* **2012**, *22*, 16640−16648.

(4) Pasero, D.; Reeves, N.; West, A. R. Co-Doped Mn_3O_4: A Possible Anode Material for Lithium Batteries. *J. Power Sources* **2005**, *141*, 156−158.

(5) Fan, Q.; Whittingham, M. S. Electrospun Manganese Oxide Nanofibers as Anodes for Lthium-Ion Batteries. *Electrochem. Solid-State Lett.* **2007**, *10*, A48−51.

(6) Shen, X. P.; Ji, Z. Y.; Miao, H. J.; Yang, J.; Chen, K. M. Hydrothermal Synthesis of $MnCO_3$ Nanorods and Their Thermal Transformation into Mn_2O_3 and Mn_3O_4 Nanorods with Single Crystalline Structure. *J. Alloys Compd.* **2011**, *509*, 5672−5676.

(7) Gao, J.; Lowe, M. A.; Abruña, H. D. Spongelike Nanosized Mn_3O_4 as A High-Capacity Anode Material for Rechargeable Lithium Batteries. *Chem. Mater.* **2011**, *23*, 3223−3227.

(8) Wang, J. Z.; Du, N.; Wu, H.; Zhang, H.; Yu, J. X.; Yang, D. R. Order-Aligned Mn_3O_4 Nanostructures as Super High-Rate Electrodes for Rechargeable Lithium-Ion Batteries. *J. Power Sources* **2013**, *222*, 32−37.

(9) Bai, Z. C.; Fan, N.; Ju, Z. C.; Guo, C. L.; Qian, Y. T.; Tang, B.; Xiong, S. L. Facile Synthesis of Mesoporous Mn_3O_4 Nanotubes and Their Excellent Performance for Lithium-Ion Batteries. *J. Mater. Chem. A* **2013**, *1*, 10985−10990.

(10) Huang, S. Z.; Jin, J.; Cai, Y.; Li, Y.; Tan, H. Y.; Wang, H. E.; Tendeloo, G. V.; Su, B. L. Engineering Single Crystalline Mn_3O_4 Nanooctahedra with Exposed Highly Active {011} Facets for High Performance Lithium Ion Batteries. *Nanoscale* **2014**, *6*, 6819−6827.

(11) Hao, Q.; Wang, J. P.; Xu, C. X. Facile Preparation of Mn_3O_4 Octahedra and Their Long-Term Cycle Life as an Anode Material for Li-Ion Batteries. *J. Mater. Chem. A* **2014**, *2*, 87−93.
(12) Jian, G. Q.; Xu, Y. H.; Lai, L. C.; Wang, C. S.; Zachariah, M. R. Mn_3O_4 Hollow Spheres for Lithium-Ion Batteries with High Rate and Capacity. *J. Mater. Chem. A* **2014**, *2*, 4627−4632.
(13) Choi, S. H.; Kang, Y. C. Using Simple Spray Pyrolysis to Prepare Yolk−Shell-Structured ZnO−Mn_3O_4 Systems with the Optimum Composition for Superior Electrochemical Properties. *Chem.—Eur. J.* **2014**, *20*, 3014−3018.
(14) Dubal, D. P.; Holze, R. High Capacity Rechargeable Battery Electrode Based on Mesoporous Stacked Mn_3O_4 Nanosheets. *RSC Adv.* **2012**, *2*, 12096−12100.
(15) Bai, Z. C.; Zhang, X. Y.; Zhang, Y. W.; Guo, C. L.; Tang, B. Facile Synthesis of Mesoporous Mn_3O_4 Nanorods as A Promising Anode Material for High Performance Lithium-Ion Batteries. *J. Mater. Chem. A* **2014**, DOI: 10.1039/C4TA03532A.
(16) Luo, S.; Wu, H. C.; Wu, Y.; Jiang, K. L.; Wang, J. P.; Fan, S. S. Mn_3O_4 Nanoparticles Anchored on Continuous Carbon Nanotube Network as Superior Anodes for Lithium Ion Batteries. *J. Power Sources* **2014**, *249*, 463−469.
(17) Wang, Z. H.; Yuan, L. X.; Shao, Q. G.; Huang, F.; Huang, Y. H. Mn_3O_4 Nanocrystals Anchored on Multi-Walled Carbon Nanotubes as High-Performance Anode Materials for Lithium-Ion Batteries. *Mater. Lett.* **2012**, *80*, 110−113.
(18) Lavoie, N.; Malenfant, P. R. L.; Courtel, F. M.; Abu-Lebdeh, Y.; Davidson, I. J. High Gravimetric Capacity and Long Cycle Life in Mn_3O_4/Graphene Platelet/LiCMC Composite Lithium-Ion Battery Anodes. *J. Power Sources* **2012**, *213*, 249−254.
(19) Liu, S. Y.; Xie, J.; Zheng, Y. X.; Cao, G. S.; Zhu, T. J.; Zhao, X. B. Nanocrystal Manganese Oxide (Mn_3O_4, MnO) Anchored on Graphite Nanosheet with Improved Electrochemical Li-Storage Properties. *Electrochim. Acta* **2012**, *66*, 271−278.
(20) Cheekati, S. L.; Xing, Y.; Zhuang, Y.; Huang, H. Graphene Platelets and Their Manganese Composites for Lithium Ion Batteries. *ECS Trans.* **2011**, *33*, 23−32.
(21) Kim, H.; Kim, S.-W.; Hong, J.; Park, Y.-U.; Kang, K. Electrochemical and Ex-Situ Analysis on Manganese Oxide/Grapheme Hybrid Anode for Lithium Rechargeable Batteries. *J. Mater. Res.* **2011**, *26*, 2665−2671.
(22) Li, L.; Guo, Z. P.; Du, A. J.; Liu, H. K. Rapid Microwave-Assisted Synthesis of Mn_3O_4−Graphene Nanocomposite and Its Lithium Storage Properties. *J. Mater. Chem.* **2012**, *22*, 3600−3605.
(23) Zhao, C. J.; Chou, S. L.; Wang, Y. X.; Zhou, C. F.; Liu, H. K.; Dou, S. X. A Facile Route to Synthesize Transition Metal Oxide/Reduced Graphene Oxide Composites and Their Lithium Storage Performance. *RSC Adv.* **2013**, *3*, 16597−16603.
(24) Nam, I.; Kim, N. D.; Kim, G.-P.; Park, J.; Yi, J. One Step Preparation of Mn_3O_4/Graphene Composites for Use as an Anode in Li Ion Batteries. *J. Power Sources* **2013**, *244*, 56−62.
(25) Chen, C.; Jian, H.; Fu, X. X.; Ren, Z. M.; Yan, M.; Qian, G. D.; Wang, Z. Y. Facile Synthesis of Graphene-Supported Mesoporous Mn_3O_4 Nanosheets with a High-Performance in Li-Ion Batteries. *RSC Adv.* **2014**, *4*, 5367−5370.
(26) Wang, H. L.; Cui, L. F.; Yang, Y.; Casalongue, H. S.; Robinson, J. T.; Liang, Y. Y.; Cui, Y.; Dai, H. J. Mn_3O_4−Graphene Hybrid as a High-Capacity Anode Material for Lithium Ion Batteries. *J. Am. Chem. Soc.* **2010**, *132*, 13978−13980.
(27) Park, S.-K.; Jin, A. H.; Yu, S.-H.; Ha, J.; Jang, B.; Bong, S.; Woo, S.; Sung, Y.-E.; Piao, Y. In Situ Hydrothermal Synthesis of Mn_3O_4 Nanoparticles on Nitrogen-Doped Graphene as High-Performance Anode Materials for Lithium Ion Batteries. *Electrochim. Acta* **2014**, *120*, 452−459.
(28) Wang, L.; Li, Y. H.; Han, Z. D.; Chen, L.; Qian, B.; Jiang, X. F.; Pinto, J.; Yang, G. Composite Structure and Properties of Mn_3O_4/Grapheme Oxide and Mn_3O_4/Grapheme. *J. Mater. Chem. A* **2013**, *1*, 8385−8397.
(29) Chae, C.; Kim, J. H.; Kim, J. M.; Sun, Y.-K.; Lee, J. K. Highly Reversible Conversion-Capacity of MnO_x-Loaded Ordered Mesoporous Carbon Nanorods for Lithium-Ion Battery Anodes. *J. Mater. Chem.* **2012**, *22*, 17870−17877.
(30) Ji, L. W.; Medford, A. J.; Zhang, X. W. Porous Carbon Nanofibers Loaded with Manganese Oxide Particles: Formation Mechanism and Electrochemical Performance as Energy-Storage Materials. *J. Mater. Chem.* **2009**, *19*, 5593−5601.
(31) Yang, G.; Li, Y. H.; Ji, H. M.; Wang, H. Y.; Gao, P.; Wang, L.; Liu, H. D.; Pinto, J.; Jiang, X. F. Influence of Mn Content on the Morphology and Improved Electrochemical Properties of Mn_3O_4| MnO@Carbon Nanofiber as Anode Material for Lithium Batteries. *J. Power Sources* **2012**, *216*, 353−362.
(32) Ji, L. W.; Zhang, X. W. Manganese Oxide Nanoparticle-Loaded Porous Carbon Nanofibers as Anode Materials for High-Performance Lithium-Ion Batteries. *Electrochem. Commun.* **2009**, *11*, 795−798.
(33) Lee, R.-C.; Lin, Y. P.; Weng, Y. T.; Pan, H.-A.; Lee, J.-F.; Wu, N.-L. Synthesis of High-Performance MnO_x/Carbon Composite as Lithium-Ion Battery Anode by a Facile Co-Precipitation Method: Effects of Oxygen Stoichiometry and Carbon Morphology. *J. Power Sources* **2014**, *253*, 373−380.
(34) Wang, C. B.; Yin, L. W.; Xiang, D.; Qi, Y. X. Uniform Carbon Layer Coated Mn_3O_4 Nanorod Anodes with Improved Reversible Capacity and Cyclic Stability for Lithium Ion Batteries. *ACS Appl. Mater. Interfaces* **2012**, *4*, 1636−1642.
(35) Kang, X. H.; Utsunomiya, H.; Achiha, T.; Ohzawa, Y.; Nakajima, T.; Mazej, Z.; Žemva, B.; Endo, M. Effect of Conductive Additives and Surface Fluorination on The Electrochemical Properties of Lithium Titanate ($Li_{4/3}Ti_{5/3}O_4$). *J. Electrochem. Soc.* **2010**, *157*, A437−442.
(36) Zheng, X. D.; Dong, C. C.; Huang, B.; Lu, M. Effects of Conductive Carbon on the Electrochemical Performances of $Li_4Ti_5O_{12}$/C Composites. *Int. J. Electrochem. Sci.* **2012**, *7*, 9869−9880.
(37) Kagesawa, K.; Hosono, E.; Okubo, M.; Kikkawa, J.; Nishio-Haman, D.; Kudoa, T.; Zhou, H. S. VGCF-Core@$LiMn_{0.4}Fe_{0.6}PO_4$-Sheath Heterostructure Nanowire for High Rate Li-Ion Batteries. *Cryst. Eng. Commun.* **2013**, *15*, 6638−6640.
(38) Kagesawa, K.; Hosono, E.; Okubo, M.; Nishio-Hamane, D.; Kudo, T.; Zhou, H. S. Electrochemical Properties of $LiMn_xFe_{1-x}PO_4$ (x = 0, 0.2, 0.4, 0.6, 0.8, and 1.0)/Vapor Grown Carbon Fiber Core-Sheath Composite Nanowire Synthesized by Electrospinning Method. *J. Power Sources* **2014**, *248*, 615−620.
(39) Xu, S. M.; Hessel, C. M.; Ren, H.; Yu, R. B.; Jin, Q.; Yang, M.; Zhao, H. J.; Wang, D. α-Fe_2O_3 Multi-Shelled Hollow Microspheres for Lithium Ion Battery Anodes with Superior Capacity and Charge Retention. *Energy Environ. Sci.* **2014**, *7*, 632−637.
(40) Su, D. W.; Ford, M.; Wang, G. X. Mesoporous NiO Crystals with Dominantly Exposed {110} Reactive Facets for Ultrafast Lithium Storage. *Sci. Rep.* **2012**, *2*, 924−931.
(41) Wang, X.; Wu, X. L.; Guo, Y. G.; Zhong, Y. T.; Cao, X. Q.; Ma, Y.; Yao, J. N. Synthesis and Lithium Storage Properties of Co_3O_4 Nanosheet-Assembled Multishelled Hollow Spheres. *Adv. Funct. Mater.* **2010**, *20*, 1680−1686.
(42) Fang, X. P.; Lu, X.; Guo, X. W.; Mao, Y.; Hu, Y. S.; Wang, J. Z.; Wang, Z. X.; Wu, F.; Liu, H. K.; Chen, L. Q. Electrode Reactions of Manganese Oxides for Secondary Lithium Batteries. *Electrochem. Commun.* **2010**, *12*, 1520−1523.
(43) Lowe, M. A.; Gao, J.; Abruña, H. D. In Operando X-ray Studies of the Conversion Reaction in Mn_3O_4 Lithium Battery Anodes. *J. Mater. Chem. A* **2013**, *1*, 2094−2103.
(44) Yonekura, D.; Iwama, E.; Ota, N.; Muramatsu, M.; Saito, M.; Orikasa, Y.; Naoi, W.; Naoi, K. Progress of the Conversion Reaction of Mn_3O_4 Particles as a Function of the Depth of Discharge. *Phys. Chem. Chem. Phys.* **2014**, *16*, 6027−6032.
(45) Laruelle, S.; Grugeon, S.; Poizot, P.; Dolle, M.; Dupont, L.; Tarascon, J.-M. On the Origin of the Extra Electrochemical Capacity Displayed by MO/Li Cells at Low Potential. *J. Electrochem. Soc.* **2002**, *149*, A627−634.
(46) Grugeon, S.; Laruelle, S.; Dupont, L.; Tarascon, J.-M. An Update on the Reactivity of Nanoparticles Co-Based Compounds towards Li. *Solid State Sci.* **2003**, *5*, 895−904.

(47) Guo, J. C.; Liu, Q.; Wang, C. S.; Zachariah, M. R. Interdispersed Amorphous MnO_x–Carbon Nanocomposites with Superior Electrochemical Performance as Lithium-Storage Material. *Adv. Funct. Mater.* **2012**, *22*, 803–811.
(48) Sun, Y. M.; Hu, X. L.; Luo, W.; Xia, F. F.; Huang, Y. H. Reconstruction of Conformal Nanoscale MnO on Graphene as a High-Capacity and Long-Life Anode Material for Lithium Ion Batteries. *Adv. Funct. Mater.* **2013**, *23*, 2436–2444.